



Protostellar collapse induced by compression - II. Rotation and fragmentation

Patrick Hennebelle, A. P. Whitworth, S.-H. Cha, S. P. Goodwin

► To cite this version:

Patrick Hennebelle, A. P. Whitworth, S.-H. Cha, S. P. Goodwin. Protostellar collapse induced by compression - II. Rotation and fragmentation. Monthly Notices of the Royal Astronomical Society, 2004, 348, pp.687-701. 10.1111/j.1365-2966.2004.07378.x . hal-03785679

HAL Id: hal-03785679

<https://hal.science/hal-03785679>

Submitted on 29 Sep 2022

HAL is a multi-disciplinary open access archive for the deposit and dissemination of scientific research documents, whether they are published or not. The documents may come from teaching and research institutions in France or abroad, or from public or private research centers.

L'archive ouverte pluridisciplinaire **HAL**, est destinée au dépôt et à la diffusion de documents scientifiques de niveau recherche, publiés ou non, émanant des établissements d'enseignement et de recherche français ou étrangers, des laboratoires publics ou privés.

Protostellar collapse induced by compression – II. Rotation and fragmentation

P. Hennebelle,^{1,2★} A. P. Whitworth,^{1★} S.-H. Cha^{1,3} and S. P. Goodwin¹

¹*Department of Physics & Astronomy, Cardiff University, PO Box 913, 5 The Parade, Cardiff CF24 3YB*

²*Laboratoire de radioastronomie millimétrique, UMR 8112 du CNRS, École normale supérieure et Observatoire de Paris, 24 rue Lhomond, 75231 Paris Cedex 05, France*

³*Department de Physique, Université de Montreal, B.P. 6128 Succ. Centre-Ville, Montreal, Quebec H3C 3J7, Canada*

Accepted 2003 November 4. Received 2003 October 20; in original form 2003 May 6

ABSTRACT

We investigate numerically and semi-analytically the collapse of low-mass, rotating prestellar cores. Initially, the cores are in approximate equilibrium with low rotation (the initial ratio of thermal to gravitational energy is $\alpha_0 \simeq 0.5$, and the initial ratio of rotational to gravitational energy is $\beta_0 = 0.02$ – 0.05). They are then subjected to a steady increase in external pressure. Fragmentation is promoted – in the sense that more protostars are formed – both by more rapid compression, and by higher rotation (larger β_0).

In general, the large-scale collapse is non-homologous, and follows the pattern described by Hennebelle et al. (Paper I) for non-rotating clouds, namely a compression wave is driven into the cloud, thereby increasing the density and the inflow velocity. The effects of rotation become important at the centre, where the material with low angular momentum forms a central primary protostar (CPP), whilst the material with higher angular momentum forms an accretion disc around the CPP. More rapid compression drives a stronger compression wave and delivers material more rapidly into the outer parts of the disc. Consequently, (i) there is more mass in the outer parts of the disc; (ii) the outer parts of the disc are denser (because the density of the material running into the accretion shock at the edge of the disc is higher); and (iii) there is less time for the gravitational torques associated with symmetry breaking to redistribute angular momentum and thereby facilitate accretion on to the CPP. The combination of a massive, dense outer disc and a relatively low-mass CPP renders the disc unstable against fragmentation, and leads to the formation of one or more secondary protostars. At their inception, these secondary protostars are typically four or five times less massive than the CPP.

For very rapid compression there is no CPP and the disc becomes more like a ring, which then fragments into two or three protostars of comparable mass.

For more rapid rotation (larger β_0), the outer disc is even more massive in comparison to the CPP, even more extended, and therefore even more prone to fragment.

Key words: gravitation – hydrodynamics – waves – stars: formation – ISM: clouds.

1 INTRODUCTION

It is now well established that stars form in dense cores embedded in molecular clouds (see, for example, André, Ward-Thompson & Barsony 2000). However, the conditions under which these cores form, become unstable, collapse and fragment are still a matter of debate.

In a previous study, Hennebelle et al. (2003, Paper I) have investigated the possibility that the collapse of a prestellar core is driven

from the outside by an increase in the external pressure. This model seems to reproduce many of the key features observed in nearby star-forming cores; in particular, (i) during the pre-stellar phase, the density profile is approximately flat in the centre (Abergel et al. 1996; Bacmann et al. 2000; Motte & André 2001). (ii) For slow to moderate compression rates, subsonic infall velocities develop in the outer parts of the core during the prestellar phase (Tafalla et al. 1998; Lee, Myers & Tafalla 1999; Williams et al. 1999). (iii) During the Class 0 phase, subsonic velocities persist in the outer parts of the core (Belloche et al. 2002) and transsonic velocities develop in the inner parts ($r \lesssim 2000$ au). (iv) There is an initial short phase of rapid accretion on to the central protostar (the Class 0

★E-mail: Patrick.Hennebelle@ens.fr (PH); ant@astro.cf.ac.uk (APW)

phase), followed by a longer phase of slower accretion (the Class I phase), as inferred from the studies of Greene et al. (1994), Kenyon & Hartmann (1995), Bontemps et al. (1996) and Motte & André (2001).

A question that was not addressed in Paper I is the formation of multiple protostars by fragmentation of a collapsing core. This question is critical, because it is now well established (Duquennoy & Mayor 1991; Fisher & Marcy 1992; Ghez et al. 1997) that a large fraction of stars is in binary – or higher multiple – systems (i.e. at least 50 per cent for mature solar-type stars in the field, and a higher percentage for pre-main-sequence stars in young associations).

1.1 Previous work

The gravitational fragmentation of a collapsing cloud has been investigated intensively for over two decades (see Bodenheimer et al. 2000 for a review), mostly with numerical simulations, but also by semi-analytic means. The enduring hope has been to derive a robust general theorem defining the conditions required for fragmentation, for instance, in terms of the initial ratio of thermal to gravitational energy, α_0 , and the initial ratio of rotational to gravitational energy, β_0 . However, robust theorems have proved elusive. This is in part because the parameter space of initial conditions and constitutive physics is very large. Therefore, the generality of the results obtained is hard to establish. In addition, fragmentation appears to depend sensitively on the complicated radiative-transport and thermal-inertia effects which come into play when star-forming gas switches from being approximately isothermal to being approximately adiabatic. The computational resources required to simulate this radiative transport properly are not yet available. Furthermore, all such theorems inevitably beg the question: how were the unstable initial conditions created in the first place? Here one probably has to appeal loosely to the chaotic effects of supersonic turbulence in star-forming molecular clouds (e.g. Elmegreen 2000; Padoan & Nordlund 2002).

The simplest case to treat is a spherical cloud with uniform density, solid-body rotation, and isothermal equation of state; this is sometimes called the standard model. Using semi-analytic arguments, based on the classical stability analysis of Maclaurin spheroids (Lytton 1953; Chandrasekhar 1969), Tohline (1981) concluded that all such clouds should fragment. Subsequently, Miyama, Hayashi & Narita (1984) used numerical simulations to derive a fragmentation criterion of the form $\alpha_0 \beta_0 \lesssim 0.12$. A similar criterion was obtained semi-analytically by Hachisu & Eriguchi (1984, 1985) and Miyama (1992) revised the criterion slightly to $\alpha_0 \beta_0 \lesssim 0.15$, on the basis of an analysis of the flatness and stability of rotating discs. Tsuribe & Inutsuka (1999a), again using a semi-analytic approach, took account of the non-homologous nature of collapse, and obtained a somewhat different criterion, which can be approximated by $\alpha_0 \lesssim 0.55-0.65\beta_0$. This criterion was subsequently confirmed with simulations (Tsuribe & Inutsuka 1999b).

The standard model can be modified in several interesting ways.

(i) The standard model can be modified by adding an $m = 2$ azimuthal density perturbation, i.e. $\rho(\mathbf{r}) = \rho_0 [1 + A \cos(\phi)]$, where ϕ is the azimuthal angle in spherical polar coordinates and A is the fractional amplitude of the perturbation. This perturbation is a common basis for numerical explorations of collapse and fragmentation. The standard model was first simulated by Boss & Bodenheimer (1979), who invoked a perturbation with amplitude $A = 0.5$. They found that a cloud having $\alpha_0 = 0.25$ and $\beta_0 = 0.20$ collapsed and fragmented to form a binary system. This result was reproduced by

Burkert & Bodenheimer (1993) using a more accurate code. Burkert & Bodenheimer (1993) also performed simulations with $\alpha_0 = 0.26$ and $\beta_0 = 0.16$ and with the amplitude of the perturbation set to $A = 0.5$ and $A = 0.1$. In the latter case they obtained not just a binary, but also a line of smaller fragments between the main binary components. However, Truelove et al. (1998) have demonstrated using an AMR code, that this is an artefact. If the collapse remains truly isothermal to high densities, and if the resolution is sufficiently high for the Jeans mass to be resolved at all times, the material between the binary components should not fragment. This has been confirmed by Boss et al. (2000), Sigalotti & Klapp (2001) and Kitsionas & Whitworth (2002), who followed the purely isothermal collapse to even higher density, using smoothed particle hydrodynamics (SPH) with particle splitting.

(ii) The standard model can be modified by changing the equation of state. Tohline (1981) and Miyama (1992) considered the collapse of clouds having an adiabatic equation of state, $P = K\rho^\gamma$, and concluded that the condition for fragmentation takes the form

$$\alpha_0 \beta_0^{(4-3\gamma)} \leq f(\gamma), \quad (1)$$

where, for example, $f(5/3) \simeq 0.064$. Alternatively, a barotropic equation of state can be adopted, in which the gas is isothermal at low densities (where star-forming gas is expected to be thin to its own cooling radiation), and adiabatic at high densities (where the gas is expected to be optically thick to its cooling radiation). Collapse simulations using a barotropic equation of state of this form are presented by Bonnell (1994), Bate & Burkert (1997), Boss et al. (2000) and Cha & Whitworth (2003). A barotropic equation of state of this type is also used in the simulations presented in this paper, and is discussed in Section 2.2. It is clear that treatment of the equation of state has a profound influence on the outcome of collapse. For example, Bate & Burkert (1997) show that the collapse of an initially uniform-density cloud having $\alpha_0 = 0.26$, $\beta_0 = 0.16$ and an $m = 2$, $A = 0.1$ azimuthal perturbation, *does* produce a line of small fragments between the two main binary components, *if* the barotropic equation of state described above is used (but not if the gas remains isothermal indefinitely). Perhaps the most telling result in this regard is reported by Boss et al. (2000) who simulated the collapse of a cloud with an $m = 2$, $A = 0.1$ perturbation, first using a barotropic equation of state, and then including radiation transport and an energy equation. The latter case produced a binary, whereas the former case did not, even though the variation of pressure with density was very similar in the two cases. The implication is that the subtle radiation-transport and thermal-inertia effects, which suddenly become important as isothermality gives way to adiabaticity, play a critical role in determining the pattern of fragmentation.

(iii) The standard model can be modified by imposing a density profile. Myhill & Kaula (1992), using a code which included radiation transport and an energy equation, showed that clouds with solid-body rotation, $\alpha_0 = 0.16$, $\beta_0 = 0.17$, and an $m = 2$, $A = 0.1$ or 0.5 azimuthal perturbation do not fragment during the isothermal collapse phase, if the density profile is centrally peaked (specifically $\rho \propto r^{-n}$ with $n = 1$ or 2). However, Burkert, Bate & Bodenheimer (1997) repeated the simulation with $A = 0.1$ and $n = 1$, using a barotropic equation of state. They found that after the central primary protostar condenses out, a circumstellar disc forms around it, and this disc then fragments to produce companion protostars. A number of simulations have also been performed with Gaussian density profiles (e.g. Boss & Myhill 1995; Burkert & Bodenheimer 1996; Boss 1996; Boss et al. 2000), and also with exponential profiles (Boss 1993), but there does not appear to have been a systematic

evaluation of the influence of these profiles on the outcome of collapse.

(iv) The standard model can be modified by introducing differential rotation. Myhill & Kaula (1992), again using a code which included radiation transport and an energy equation, showed that clouds with $\alpha_0 = 0.16$, $\beta_0 = 0.17$, a centrally peaked density profile ($\rho \propto r^{-n}$ with $n = 1$ or 2), and an $m = 2$, $A = 0.1$ or 0.5 azimuthal perturbation, do fragment if they have sufficient differential rotation (in contrast with the result for solid-body rotation). The tendency for differential rotation to promote fragmentation has been confirmed by Boss & Myhill (1995) and Cha & Whitworth (2003).

(v) Finally, a number of authors have explored the effect of clouds having non-spherical initial shapes. Evidently, the outcome here depends not only on α_0 (and β_0 , if there is rotation), but also on the aspect ratio of the initial configuration. Bastien (1983) simulated the collapse of isothermal, non-rotating cylindrical clouds and determined the mass per unit length required for fragmentation. This problem was revisited by Bonnell & Bastien (1991) and Bastien et al. (1991), and extended to polytropic cylinders by Arcoragi et al. (1991). Bonnell et al. (1991) explored the circumstances under which isothermal cylinders rotating about an axis perpendicular to their elongation fragment to produce binary systems, and Bonnell et al. (1992) considered isothermal cylinders rotating about an arbitrary axis. Bonnell & Bastien (1992) repeated this last study with cylinders having a density gradient along the symmetry axis, and showed that quite modest gradients were sufficient to produce binary systems with mass ratios in the range 0.1–1. Nelson & Papaloizou (1993) (see also Bonnell, Bate & Price 1996) simulated the collapse of prolate spheroids, and showed that they fragment if the mass per unit length is sufficiently high (as for cylinders), but the binary components tend to be closer because there is less mass at the ends of a prolate spheroid. Boss (1993) simulated the collapse and fragmentation of a rotating, mildly prolate cloud with an exponential density profile, and showed that the conditions for fragmentation were rather more restrictive than those obtained by Miyama et al. (1984). These results were extended to mildly prolate clouds having a Gaussian density profile and differential rotation by Boss & Myhill (1995); and to more elongated prolate clouds having a Gaussian density profile, but solid-body rotation, by Sigalotti & Klapp (1997). Boss (1996) simulated the collapse of rotating isothermal oblate spheroidal clouds and showed that fragmentation into multiple systems occurs provided $\alpha_0 < 0.4$, almost independent of β_0 . Monaghan (1994) explored the effect of vorticity on the collapse and fragmentation of ellipsoidal clouds, using numerical simulations.

1.2 Outline of the paper

In this paper we pursue further our investigation of prestellar cores where the collapse is induced by a steady increase in the external pressure. We extend the investigation to the case of rotating cores, and focus on the formation of circumstellar discs around the central primary protostars (CPPs) and the subsequent fragmentation of these discs. Our main goal is to relate the properties of the star systems formed (multiplicities and mass ratios) to the dynamics of the collapse, and hence to the parameters β_0 and ϕ , measuring –, respectively, – the initial rate of rotation and the rate of compression (see equation 8). Our model invokes initial conditions, and generates density and velocity profiles, very similar to those inferred from observations of real star-forming cores. However, without performing a large (i.e. statistically robust) ensemble of simulations, we cannot know whether it also delivers multiple systems with statistics similar to those observed.

In Section 2 we describe the numerical method we use, the constitutive physics, and the initial and boundary conditions. In Section 3, we present our results, with special attention to the large-scale velocity and density fields in the cores. Section 4 discusses the evolution of the discs that form around the central primary protostars, with particular emphasis on the fragmentation process. Section 5 summarizes our main conclusions. In the Appendix, we develop a semi-analytical description of the key features discussed in Sections 3 and 4, and estimate the time-scales influencing disc stability. We perceive this analysis as an integral part of our paper, and we have put it in an appendix purely so that those whose main interest is in the phenomenology of fragmentation can read about the results of our simulations without getting to grips with the more mathematical aspects, which give an approximate quantitative explanation for the dependence of disc stability on the initial core rotation and the rate of compression.

2 CONSTITUTIVE PHYSICS, INITIAL CONDITIONS AND NUMERICAL METHOD

2.1 Coordinates

With respect to a Cartesian coordinate system (x, y, z), the global angular momentum of the core will always be directed along the z -axis. Distance from the origin will be denoted by

$$r = (x^2 + y^2 + z^2)^{1/2}, \quad (2)$$

and distance from the rotation axis by

$$w = (x^2 + y^2)^{1/2}. \quad (3)$$

The velocity is then divided into three orthogonal components: the equatorial velocity component,

$$v_w = (xv_x + yv_y)/w; \quad (4)$$

the azimuthal velocity component,

$$v_\theta = (xv_y - yv_x)/w; \quad (5)$$

and the polar velocity component, v_z .

2.2 The equation of state

We use a barotropic equation of state (cf. Bonnell 1994), which mimics the expected thermal behaviour of star-forming gas (e.g. Tohline 1982; Masunaga & Inutsuka 2000):

$$\frac{P}{\rho} \equiv C_s^2 = C_0^2 \left[1 + \left(\frac{\rho}{\rho_0} \right)^{2/3} \right]. \quad (6)$$

Here P is the pressure, ρ is the density, and C_s is the isothermal speed of sound.

At low densities, $\rho < \rho_0 = 10^{-13} \text{ g cm}^{-3}$, $C_s \simeq C_0 = 0.19 \text{ km s}^{-1}$, corresponding to isothermal molecular gas at 10 K. The presumption is that the gas is able to radiate freely, either via molecular line radiation, or – once the density rises above approximately $10^{-19} \text{ g cm}^{-3}$ – by coupling thermally to the dust.

At high densities, $\rho > \rho_0$, $P \propto \rho^{5/3}$, corresponding to an adiabatic gas with adiabatic exponent $\gamma = 5/3$. Here the presumption is that the cooling radiation is trapped by dust opacity. We note that molecular hydrogen behaves like a monatomic gas until the temperature reaches several hundred Kelvin, because the rotational degrees of freedom are not excited at lower temperatures, and hence $\gamma = 5/3$ is the appropriate adiabatic exponent.

The switch to adiabatic behaviour at high density causes the gravitational collapse to slow down, and obviates the need to invoke sink particles (Bate et al. 1995). This allows us to capture the dynamics of the disc, and accretion from the disc on to the central protostar, much more accurately. If a sink were introduced it might seriously influence the development of spiral density waves in the disc and its patterns of fragmentation.

2.3 The initial and boundary conditions

The initial conditions are a rotating truncated Bonnor–Ebert sphere, contained by a hot rarefied intercore medium having uniform density. The Bonnor–Ebert sphere is truncated at $\xi = 6$ [i.e. at radius $R = 6 C_0 / (4\pi G \rho_c)^{1/2}$, where G is the universal gravitational constant and ρ_c is the central density]. The core mass is one solar mass and its initial radius is $\simeq 0.05$ pc. This is a reasonable representation of observed prestellar cores (e.g. André et al. 2000).

Because of its initial rotation, this configuration is not strictly in equilibrium. However, since the rotational energy is only a few per cent of the gravitational potential energy ($\beta_0 = 0.02$ – 0.05), it is very close to equilibrium.

Molecular-line observations of dense cores (Goodman et al. 1993) suggest that typically the ratio of rotational to gravitational energy is $\beta_0 \simeq 0.02$. We therefore adopt this value for most of our simulations. In addition, we consider $\beta_0 = 0.05$, in order to explore the dependence on β_0 .

The rotation profile is obtained by assuming that the original core had uniform density and rotated as a solid-body, and that angular momentum was then conserved minutely, whilst the core evolved from this original uniform-density state to our centrally condensed initial conditions. This means that our initial configuration is rotating differentially at the outset.

At $t = 0$, the temperature of the intercore medium is increased in such a way that its pressure satisfies

$$P(t) = P_0 + \dot{P}t. \quad (7)$$

We define

$$\phi = \frac{P_0 / \dot{P}}{R_0 / C_0}. \quad (8)$$

Thus ϕ is the ratio between the time-scale on which the intercore pressure doubles and the sound-crossing time of the core. A low value of ϕ means rapid compression, whereas a high value means slow compression.

2.4 Numerical method

The numerical method used is very similar to that described in Paper I. We use a standard smoothed particle hydrodynamics code (e.g. Monaghan 1992) in combination with tree-code gravity. There are three types of particle: the core particles, which experience both hydrodynamic and gravitational forces; the intercore particles, which experience only hydrodynamic forces; and the boundary particles, which are passive. There are $\sim 10^5$ core particles, $\sim 5 \times 10^4$ intercore particles, and $\sim 3 \times 10^4$ boundary particles.

Since we are simulating rotating cores, the intercore and boundary particles are given an initial uniform angular velocity, so as to minimize loss of angular momentum due to friction between the core and intercore gas, and between the intercore gas and the boundary.

2.5 The Jeans condition

In a numerical simulation involving self-gravity, it is essential that the Jeans condition be obeyed, i.e. that the Jeans mass be resolved at all times (Bate & Burkert 1997; Truelove et al. 1997, 1998). The Jeans mass is $M_{\text{Jeans}} \sim 6 G^{-3/2} \rho^{-1/2} C_s^3$, and the minimum resolvable mass in SPH is $M_{\text{resolved}} \sim \mathcal{N}_{\text{neib}} m$, where $\mathcal{N}_{\text{neib}} \simeq 50$ is the mean number of neighbours within the smoothing kernel of a typical SPH particle, and m is the mass of a single SPH particle. Thus the Jeans condition can be written as an upper limit on the mass of a single SPH particle,

$$m < m_{\text{max}} \sim \frac{6C_s^3}{\mathcal{N}_{\text{neib}} G^{3/2} \rho^{1/2}}. \quad (9)$$

From equation (6) we see that the minimum value of $C_s^3 / \rho^{1/2}$ is $2^{3/2} C_0^3 / \rho_0^{1/2}$. Hence the Jeans condition is always satisfied as long as

$$m < m_{\text{max}} \sim \frac{2^{3/2} 6C_0^3}{\mathcal{N}_{\text{neib}} G^{3/2} \rho_0^{1/2}} \sim 2.5 \times 10^{-4} M_{\odot}. \quad (10)$$

Since we model a $1 M_{\odot}$ core with 10^5 equal-mass particles, we have $m = 10^{-5} M_{\odot}$. Consequently, the Jeans condition is easily satisfied, and this ensures that the fragmentation which occurs in our simulations is not a consequence of poor numerical resolution. In addition, we have repeated all the simulations presented here with $\sim 5 \times 10^4$ core particles, and shown that the results are statistically unchanged; precise agreement is not expected, since fragmentation is seeded by particle noise, and particle noise is dependent on the number of particles.

2.6 Angular momentum conservation

Although the SPH equations ensure conservation of the global angular momentum, angular momentum is not necessarily well conserved locally. In particular, for the simulations involving slow compression, the duration of the pre-collapse phase can be as long as three or four free-fall times, and significant unphysical transport of angular momentum can occur during this time. By unphysical transport of angular momentum we mean the transport which arises before azimuthal symmetry is broken, due to differential rotation and the friction caused by artificial and numerical viscosity.

In order to limit this effect, we invoke the Balsara switch (Balsara 1995), i.e. we multiply the artificial viscosity term by the factor

$$\frac{|\nabla \cdot \mathbf{v}|}{|\nabla \cdot \mathbf{v}| + |\nabla \wedge \mathbf{v}| + C_s / (10^3 h)}. \quad (11)$$

Even with this factor (equation 11), we find that angular momentum loss from the inner parts of the core can be significant. For example, with the slowest compression rate that we treat ($\phi = 3$, see the next section), the 10 000 densest particles (10 per cent of the total number of particles) have lost approximately 20 per cent of their initial angular momentum by the time the inner disc starts to form; in contrast, the total cloud angular momentum is conserved to within a few per cent. For the intermediate compression rate ($\phi = 1$), the 10 000 densest particles have lost approximately 10 per cent of their initial angular momentum by the time the inner disc starts to form, and for the faster compressions ($\phi \lesssim 0.3$), this figure is $\lesssim 5$ per cent.

In order to check that our results are not significantly altered by unphysical transport of angular momentum, we have repeated several simulations with local conservation of angular momentum imposed on all particles having density $\rho < 10^{-4} \rho_0$. This ensures

that angular momentum is conserved locally as long as the core remains axisymmetric. Physical transport of angular momentum, due to the gravitational torques which accompany symmetry-breaking instabilities, does not occur until the disc density exceeds $10^{-4}\rho_0$ (see Section 4).

In order to impose local conservation of angular momentum, at each time-step and for each particle i , we calculate the velocity by solving the equation of motion, and then we extract the azimuthal component, $v_{\theta,i}(t)$. $v_{\theta,i}(t)$ is then recalculated so as to enforce local conservation of angular momentum, i.e.

$$v_{\theta,i}(t) = v_{\theta,i}(0)w_i(0)/w_i(t). \quad (12)$$

In these simulations the angular momentum loss of the 10 000 densest particles is reduced to approximately 5 per cent, before symmetry breaking occurs. However, in terms of the growth and fragmentation of the central disc, there is no significant difference from the simulations where local conservation of angular momentum is not imposed.

3 COLLAPSE OF A ROTATING CLOUD INDUCED BY EXTERNAL COMPRESSION

In this section we present the results of two simulations involving a core which initially has $\beta_0 = 0.02$. In the first simulation, the core is compressed slowly ($\phi = 3$), and in the second it is compressed rapidly ($\phi = 0.3$). We limit the discussion here to a description of the density and velocity fields which develop on scales much larger than the central primary protostar or the rotationally supported disc which forms around it. A detailed discussion of the structure and evolution of the disc will be given in Section 4. Since the initial rotation energy is small ($\beta_0 = 0.02$), rotation has little effect on the large-scale fields under discussion in this section, and most of the dynamical effects are the same as for the non-rotating cores analysed in Paper I.

3.1 Slow compression ($\phi = 3$, $\beta_0 = 0.02$)

In Fig. 1 we show results for slow compression, $\phi = 3$. Four times are shown: $t = 0.560$ Myr (thin full line) is significantly before the central primary protostar forms; $t = 0.610$ Myr (dotted line) is when the maximum density first reaches ρ_0 , just before the central primary protostar forms; $t = 0.611$ Myr (dashed line) is after the central primary protostar has formed and the disc has just started to form; $t = 0.615$ Myr (dot-dash line) is approximately 4000 yr after the disc starts to form. Plots (a) and (b) are log–log plots showing, respectively, the run of density along the equatorial plane [$\rho(w, z = 0)$] and the run of density along the polar axis [$\rho(w = 0, z)$]; for reference, the thick full line on these plots shows the density of the singular isothermal sphere (hereafter SIS),

$$\rho_{\text{SIS}} = \frac{C_0^2}{2\pi Gr^2}. \quad (13)$$

Plots (c)–(e) are log–linear plots showing, respectively, the run of equatorial velocity [$v_w(w, z = 0)$], the run of polar velocity [$v_z(w = 0, z)$], and the run of azimuthal velocity in the equatorial plane [$v_\theta(w, z = 0)$].

In the outer parts of the core ($r > 0.03$ pc), the density profile is very close to the SIS, both along the equator, and along the pole. However, towards the centre, the equatorial density [$\rho(w, z = 0)$] gradually becomes larger than the SIS density, and the polar density [$\rho(w = 0, z)$] gradually becomes smaller than the SIS density. The reasons for this are analysed in the Appendix. In preparation for

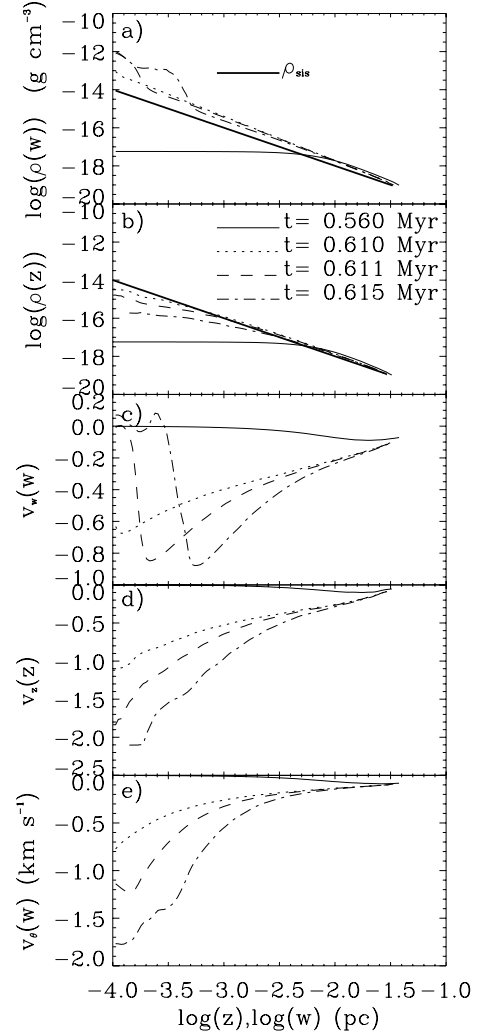


Figure 1. Slow compression ($\phi = 3$) of a rotating cloud with $\beta_0 = 0.02$. (a) shows $\log_{10}[\rho(w, z = 0)/\text{g cm}^{-3}]$ against $\log_{10}[w/\text{pc}]$. (b) shows $\log_{10}[\rho(w = 0, z)/\text{g cm}^{-3}]$ against $\log_{10}[z/\text{pc}]$. (c) shows $v_w(w, z = 0)/\text{km s}^{-1}$ against $\log_{10}[w/\text{pc}]$. (d) shows $v_z(w = 0, z)/\text{km s}^{-1}$ against $\log_{10}[z/\text{pc}]$. (e) shows $v_\theta(w, z = 0)/\text{km s}^{-1}$ against $\log_{10}[w/\text{pc}]$. Four times are shown: $t = 0.560$ Myr (thin full line) is significantly before the central primary protostar forms; $t = 0.610$ Myr (dotted line) is when the density first reaches ρ_0 , just before the central primary protostar forms; $t = 0.611$ Myr (dashed line) is after the central primary protostar has formed and the disc has just started to form; $t = 0.615$ Myr (dot-dash line) is approximately 4000 yr after the disc starts to form. For reference, the thick full line on plots (a) and (b) shows the density of the singular isothermal sphere, $C_0^2/2\pi Gr^2$ (see equation 13).

the analysis in the Appendix, Fig. 2(a) shows the equatorial density profile at $t = 0.610$, when the density first exceeds ρ_0 , normalized to the density of the singular isothermal sphere (thin dashed line). In addition, we have simulated the collapse of the same core (Bonnor–Ebert sphere with $\xi = 6$), compressed at the same rate ($\phi = 3$), but with no rotation ($\beta_0 = 0$); the radial density profile obtained in this case, when the density first exceeds ρ_0 at time $t = 0.497$, is shown as a dotted line (the thick dashed line on this plot is defined in the Appendix). The equatorial density profile of the non-rotating core is higher than the density profile of the SIS, and the equatorial density profile of the rotating core is higher still, particularly towards the centre.

In Fig. 1, the equatorial density increases abruptly (by a factor 10–20) inside $r \simeq 2 \times 10^{-4}$ pc at $t = 0.611$ Myr, and inside

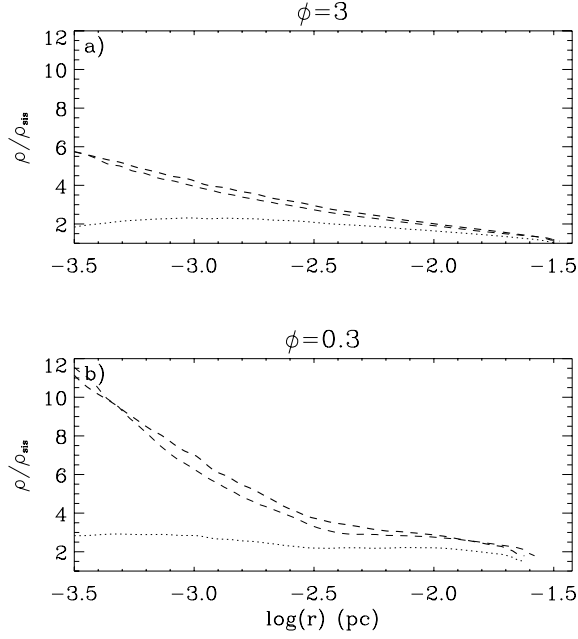


Figure 2. These plots show equatorial density profiles, $\rho(w, z = 0)$, normalized to the density profile of the singular isothermal sphere (see equation 13), for the two cases: (a) $\phi = 3$, i.e. slow compression; and (b) $\phi = 0.3$, i.e. fast compression. The thin dashed line gives the equatorial density profile when the density first exceeds ρ_0 , close to the moment the central primary protostar forms, and before the disc starts to form; in case (a) this moment is $t = 0.610$ Myr, and in case (b) it is 0.2585 Myr. The dotted line gives the equatorial density profile, again when the density first exceeds ρ_0 close to the moment the central primary protostar forms, but for a non-rotating core (all the other initial conditions of the core are the same); in case (a) this moment is $t = 0.497$ Myr, in case (b) it is 0.225 Myr. The thick dashed line gives the product of the density of the non-rotating cloud (dotted line) and the factor $1 + (v_\theta/C_s)^2/2$ (see equation 10).

$r \simeq 5 \times 10^{-4}$ pc at $t = 0.615$ Myr. This abrupt density increase marks the accretion shock at the outer edge of the growing disc.

The inward velocity at the edge of the core is similar at the poles and around the equator, ranging from ~ 0.07 km s $^{-1}$ at $t = 0.560$ Myr to ~ 0.11 km s $^{-1}$ at $t > 0.610$ Myr. Towards the centre, the magnitude of the polar velocity $|v_z(w = 0, z)|$ increases more rapidly than the magnitude of the equatorial velocity $|v_w(w, z = 0)|$, due to centrifugal acceleration. Interior to 0.01 pc, $|v_z(w = 0, z)|$ is approximately twice $|v_w(w, z = 0)|$, until the material flowing inwards close to the equator encounters the outer boundary of the disc. At this point, $|v_w(w, z = 0)|$ decreases abruptly in the accretion shock at the disc boundary. The maximum value of $|v_w(w, z = 0)|$, just before the material hits the disc boundary, is approximately constant at a value ~ 0.85 km s $^{-1}$. In contrast, the maximum polar velocity increases continuously.

This simulation has been repeated with the procedure described in Section 2.6 which forces local conservation of angular momentum. The results are very similar, the only difference being that the maximum value of $|v_w(w, z = 0)|$, just before the material hits the disc boundary, is ~ 0.75 km s $^{-1}$ instead of ~ 0.85 km s $^{-1}$.

3.2 Fast compression ($\phi = 0.3$, $\beta_0 = 0.02$)

In Fig. 3 we show the results for fast compression, $\phi = 0.3$. Four times are shown: $t = 0.240$ Myr (thin full line) is significantly before the central primary protostar forms; $t = 0.2585$ Myr (dotted line) is

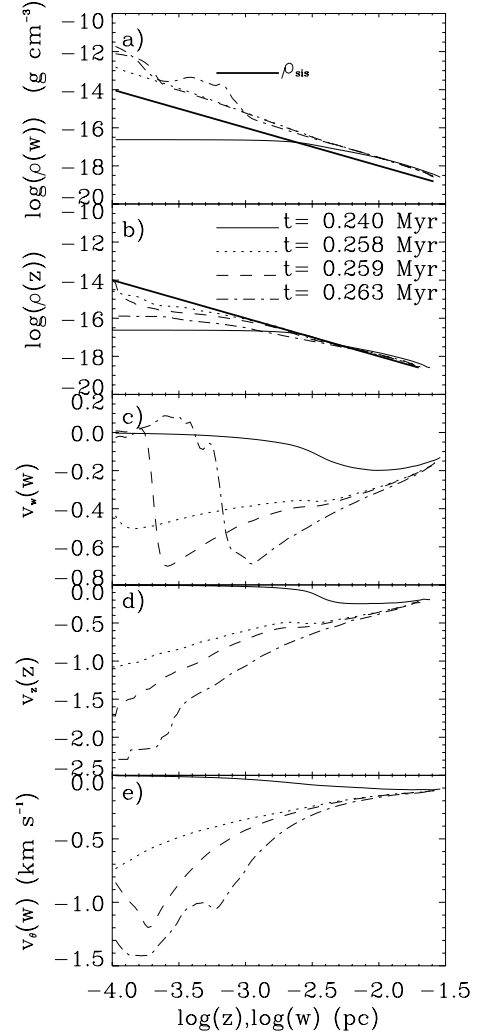


Figure 3. The same as Fig. 1, but for fast compression ($\phi = 0.3$) of a rotating cloud with $\beta_0 = 0.02$. Four times are shown: $t = 0.240$ Myr (thin full line) is significantly before the primary protostar forms; $t = 0.2585$ Myr (dotted line) is when the density first reaches ρ_0 , just before the central primary protostar forms; $t = 0.2593$ Myr (dashed line) is after the central primary protostar has formed and the disc has just started to form; and $t = 0.2625$ Myr (dot-dash line) is approximately 3000 yr after the disc starts to form. The thick line on plots (a) and (b) is the density of a singular isothermal sphere.

when the maximum density first reaches ρ_0 just before the central primary protostar forms; $t = 0.2593$ Myr (dashed line) is after the central primary protostar has formed and the disc has just started to form; and $t = 0.2625$ Myr (dot-dash line) is approximately 3000 yr after the disc starts to form. Some significant differences from the case $\phi = 3$ can be seen in the density and velocity profiles.

First, due to the more rapidly increasing external pressure, the core is more compact; the cloud radius is approximately 0.035 pc for $\phi = 3$ whereas it is approximately 0.025 pc for $\phi = 0.3$ (see Figs 1 and 3). Consequently, the equatorial density $\rho(w, z = 0)$ is higher than for $\phi = 3$ (typically by a factor ~ 1.5 – 2). In contrast, the polar density is more or less the same as for the case $\phi = 3$. From Fig. 2, there appear to be two factors contributing to the increase in equatorial density with decreasing ϕ . (a) The non-rotating cloud (dotted lines) has higher equatorial density for $\phi = 0.3$ (middle panel) than for $\phi = 3$ (upper panel), so the first factor depends only on the rate of

compression, and not on the angular momentum. (b) The ratio of the rotating cloud density to the non-rotating cloud density is larger for $\phi = 0.3$ than for $\phi = 3$, so the second factor depends both on the rate of compression, and on the angular momentum. The reason for this is analysed in the Appendix.

Secondly, the inward equatorial velocity $|v_w(w, z = 0)|$ in the outer parts of the core is greater for $\phi = 0.3$ than for $\phi = 3$. For example, the edge velocity is $\sim 0.15\text{--}0.20 \text{ km s}^{-1}$ for $\phi = 0.3$ (as compared with $\sim 0.07\text{--}0.11 \text{ km s}^{-1}$ for $\phi = 3$); and at $r = 0.01 \text{ pc}$, it is $\sim 0.3\text{--}0.35 \text{ km s}^{-1}$ for $\phi = 0.3$ (as compared with $\sim 0.18\text{--}0.20 \text{ km s}^{-1}$ for $\phi = 3$). The equatorial velocity profile is also flatter than for the case $\phi = 3$, due to the compression wave. At $t = 0.2625 \text{ Myr}$, there are large fluctuations in $v_w(w, z = 0)$ at small radii ($r < 0.002 \text{ pc}$), due to the development of non-axisymmetric modes. These will be discussed further in Section 4.

4 FRAGMENTATION

In this section we focus on what happens in the central parts of the cloud, and the details of the fragmentation process.

4.1 Slow compression

Fig. 4 illustrates the development of instability in the disc which forms around the central protostar, for the case $\phi = 3$ (slow compression) and $\beta_0 = 0.02$. The left-hand column shows particle positions projected on to the $z = 0$ plane. The right-hand column shows $\log_{10}[\rho_i]$ plotted against equatorial coordinate w_i , for each particle i having density above $10^{-14} \text{ g cm}^{-3}$, and the solid line shows $\bar{\rho}(w)$, the mean density interior to radius w , as defined in equation (A31). The central density first rises above $\rho_0/3$ at $t = 0.6097 \text{ Myr}$, and the five time-steps shown correspond to 2000, 3000, 4000, 5000 and 8000 yr after this. The density and velocity fields on larger scales are illustrated in Fig. 1. Fig. 4(a) shows the disc which forms in the centre of the core around the primary protostar. At this stage its central density is approximately $3 \times 10^{-12} \text{ g cm}^{-3}$ and its edge density is approximately 10 times smaller. It is bounded by an accretion shock, where the density falls by a further factor of 10. The disc has $\beta \simeq 0.36$, but it is still apparently symmetric. The density throughout the disc has only just started to rise above $\bar{\rho}$, and therefore it is only mildly unstable according to the analysis presented in the Appendix (section A4). Symmetry breaking is first evident a few hundred years later, by which time $\beta \simeq 0.40$.

In Figs 4(b) and (c), a strong two-armed spiral pattern develops in the disc, due to spontaneous symmetry breaking, but the arms do not sweep up sufficient mass to become gravitationally unstable, and they quickly wind up. This is very reminiscent of the numerical results reported by Durisen et al. (1986), and is due to the fact that the $m = 2$ modes are the first to become dynamically unstable (Chandrasekhar 1969; Ostriker & Bodenheimer 1973). As in the numerical simulations of Durisen et al. (1986), the arms generate gravitational torques which transport angular momentum outwards through the disc, allowing the central parts to condense on to the primary protostar, and the outer parts to expand. However, the situation we simulate here differs from that modelled by Durisen et al, because the discs in our simulations are accreting from an infalling envelope. This has two fundamental consequences. First, the mass at the outer edge of the disc is continuously replenished; this effect was described by Bonnell (1994) and by Whitworth et al. (1995), who showed numerically that this process will often lead to fragmentation. Secondly, the edge of the disc is bounded by an accretion shock which compresses the gas at the edge of the disc (see Fig. 1).

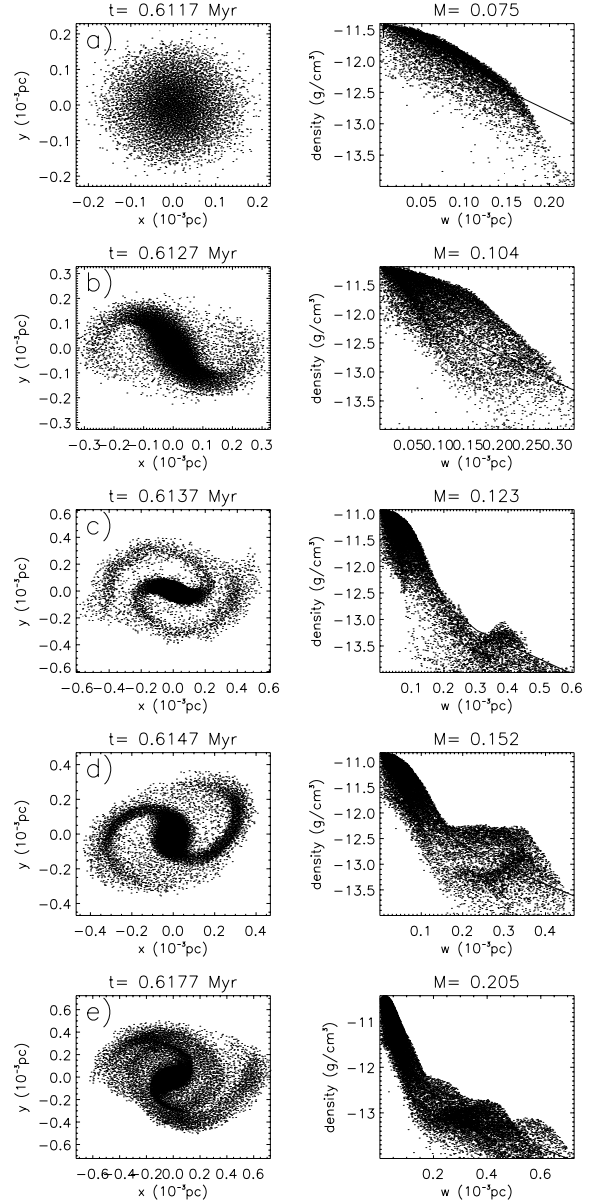


Figure 4. Disc instability in the central $\sim 10^{-3} \text{ pc}$ for $\phi = 3$ (slow compression) and $\beta_0 = 0.02$. The left-hand column shows particle positions projected on to the $z = 0$ plane. The right-hand column shows $\log_{10}[\rho_i]$ plotted against equatorial coordinate w_i , for each particle i having density above $10^{-14} \text{ g cm}^{-3}$, and the solid line shows $\bar{\rho}(w)$, the mean density interior to radius w , as defined in equation (A31). Five time-steps are shown, $t = 0.6117, 0.6127, 0.6137, 0.6147, 0.6177 \text{ Myr}$. The mass on top of the panels is in M_\odot . The density and velocity fields on larger scales are illustrated in Fig. 1. No fragmentation occurs.

We note that since the perturbations that lead to symmetry breaking are numerical noise due to the initial particle distribution, the details of the structures that form – for example, the orientation of the spiral arms – are not identical for two different realizations, i.e. two different initial particle distributions representing the same macroscopic initial conditions. However, the statistical properties – such as the numbers, masses and orbits of protostars produced – do not significantly depend on the initial particle distribution, nor do they depend significantly on the numerical resolution.

Figs 4(d) and (e) show the subsequent evolution of the disc. The disc is replenished by infalling material, and a second strong

two-armed spiral pattern develops, but again it fails to sweep up sufficient material to become gravitationally unstable. Instead, it generates gravitational torques which transport angular momentum outwards, allowing the inner material of the disc to accrete on to the central primary protostar and dispersing the outer material of the disc. No secondary protostar is formed.

4.2 Fast compression

Fig. 5 shows results for $\phi = 0.3$ (rapid compression) and $\beta_0 = 0.02$. In this case the central density first rises above $\rho_0/3$ at $t \simeq$

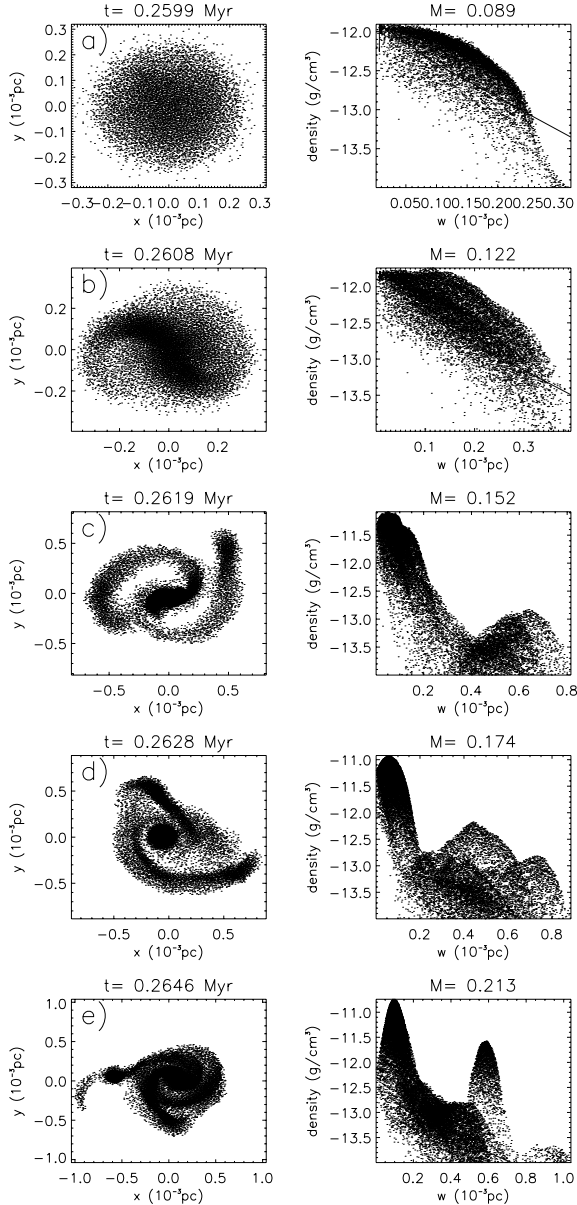


Figure 5. Disc instability in the central $\sim 2 \times 10^{-3}$ pc for $\phi = 0.3$ (rapid compression) and $\beta_0 = 0.02$. The left-hand column shows particle positions projected on to the $z = 0$ plane. The right-hand column shows $\log_{10}[\rho_i]$ plotted against equatorial coordinate w_i , for each particle i having density above 10^{-14} g cm $^{-3}$, and the solid line shows $\bar{\rho}(w)$, the mean density interior to radius w , as defined in equation (A31). Five time-steps are shown, $t = 0.2599, 0.2608, 0.2619, 0.2628, 0.2646$ Myr. The mass on top of the panels is in M_\odot . The density and velocity fields on larger scales are illustrated in Fig. 3. A second protostar condenses out of one of the spiral arms.

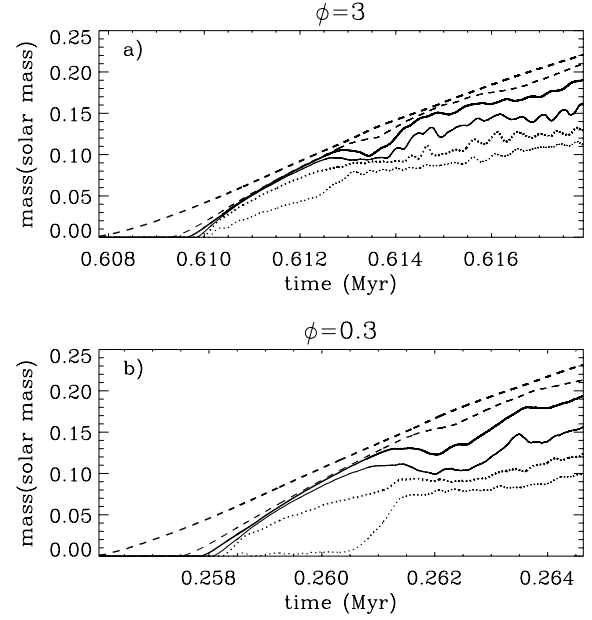


Figure 6. The mass of gas having density larger than $10 \rho_0$ (dotted line), $3 \rho_0$ (thick dotted line), $\rho_0 = 10^{-13}$ g cm $^{-3}$ (thin full line), $\rho_0/3$ (thick full line), $\rho_0/10$ (dashed line) and $\rho_0/100$ (thick dashed line), for $\phi = 3$ (a) and $\phi = 0.3$ (b).

0.2578 Myr (see Fig. 6), and the time-steps shown are 2000, 3000, 4000, 5000 and 7000 yr after this. The principal effects of more rapid compression are (i) to drive material into the disc more rapidly, thereby building up the mass of the disc more quickly, and curtailing the time the disc has to stabilize itself by redistributing angular momentum and accreting on to the central primary protostar; and (ii) to increase the density in the outer parts of the disc.¹ The result is that the central primary protostar is smaller and the disc fragments to produce a secondary protostar.

This can be seen in Fig. 5(a), which illustrates the structure of the disc just before symmetry breaking occurs. In comparison with the case $\phi = 3$, the disc here is both more massive and has a flatter density profile, i.e. the central density is lower and there is more mass in the outer parts of the disc. Consequently, the density in the outer parts is significantly higher than the mean density, and the disc is gravitationally unstable according to Condition (A33). At this stage $\beta \simeq 0.48$, and by the time symmetry breaking occurs, $\beta \simeq 0.51$.

The development of the instability is similar to the previous case, but because the outer parts of the disc are denser, the spiral arms are denser, more extended, and consequently more unstable (than for $\phi = 3$). Increasing the rate of compression does not simply accelerate the formation of the disc, but also reduces the time available for redistribution of angular momentum by symmetry breaking, thereby generating a greater ratio of disc mass to primary protostar mass.

Fig. 5(d) shows the non-linear development of the spiral arms, and in panel (e) a second object forms, located at $x \simeq -6 \times 10^{-4}$ pc and $y \simeq 1 \times 10^{-4}$ pc. At this stage ($t = 0.2646$ Myr), the mass of the

¹ We stress that this latter effect is not because the Mach number of the accretion shock is higher – the speed with which material flows into the accretion shock at the edge of the disc is not strongly dependent on the rate of compression – but because the density of the material flowing into the shock is higher for faster compression.

central primary protostar is $M_1 \simeq 0.08 M_\odot$ (75 per cent of which was already in the system at time $t = 0.2599$ Myr, i.e. before symmetry breaking started), and the mass of the newly formed secondary is $\simeq 0.02 M_\odot$ (of which 40 per cent was in the system before symmetry breaking started).

The systematic differences between the cases $\phi = 3$ (slow compression) and $\phi = 0.3$ (fast compression) are further illustrated in Fig. 6, which shows the mass of gas with density in excess of various representative thresholds ($10\rho_0$, $3\rho_0$, ρ_0 , $\rho_0/3$, $\rho_0/10$ and $\rho/100$), as a function of time. Symmetry breaking occurs at $t = 0.612$ Myr for $\phi = 3$, and at $t = 0.2632$ Myr for $\phi = 0.3$. The maxima exhibited by the curves for intermediate thresholds (ρ_0 , thin full line; $\rho_0/3$, thick full line) are due to expansion of the disc, caused by symmetry breaking and redistribution of angular momentum. Fig. 6(a) shows that for $\phi = 3$, when symmetry breaking occurs, the density in the disc is relatively low, and a large fraction of the system mass is already in the central primary protostar, thereby stabilizing the disc. Conversely, panel (b) shows that for $\phi = 0.3$, when symmetry breaking occurs, the density in the disc is relatively high, and a much smaller fraction of the system mass is in the central primary protostar. Panel (b) also shows how the transport of angular momentum in the disc is accelerated once the secondary protostar forms at $t = 0.2632$ Myr.

4.3 Faster compression: ring formation

Fig. 7 shows results for $\phi = 0.1$, $\beta_0 = 0.02$. The behaviour is very different from the previous cases. Even before the maximum density approaches $\rho_0 = 10^{-13} \text{ g cm}^{-3}$, a ring forms, and there is no central primary protostar. Ring formation is attributable to a combination of factors.

First, there is a centrifugal barrier, and this creates the rarefaction at the centre of the ring. The dynamics of ring formation due to a centrifugal barrier have been analysed by Tohline (1980), on the basis of pressureless collapse in an external potential. Bonnell & Bate (1994) have also noted the transition from disc formation to ring formation, as the speed of collapse increases. In their case the speed of collapse was increased by reducing the initial ratio of thermal to gravitational energy in the cloud. Cha & Whitworth (2003) have explored the influence of differential rotation on ring formation. In order to understand better the origin of the ring, we have monitored where the material impinging on the centre of a core originates, and we find the following distinction. For relatively slow compression ($\phi \gtrsim 0.3$, Sections 4.1 and 4.2), the material which first impinges on the centre of the core was initially concentrated near the rotation axis (z -axis). Therefore, this material has very low specific angular momentum (as compared with material originating further from the rotation axis). This is why it reaches the centre first (it experiences least centrifugal acceleration than material originating further from the rotation axis), and why on reaching the centre it can stay there to form the central primary protostar. In contrast, for faster compression ($\phi \lesssim 0.1$, this section), the compression wave is stronger, and drives material into the centre more isotropically. As a result, most of the material impinging on the centre originates far from the rotation axis and therefore has too much angular momentum to reach the centre, so there is a central rarefaction – and hence a ring is formed.

Secondly, the material delivered into the outer parts of the nascent disc is compressed to high density by the accretion shock at the edge of the disc. In order to confirm this effect, we have extracted the ring displayed in Fig. 7(b) (i.e. we have selected particles having density larger than $\rho_0/10$) and we have then let the ring evolve in

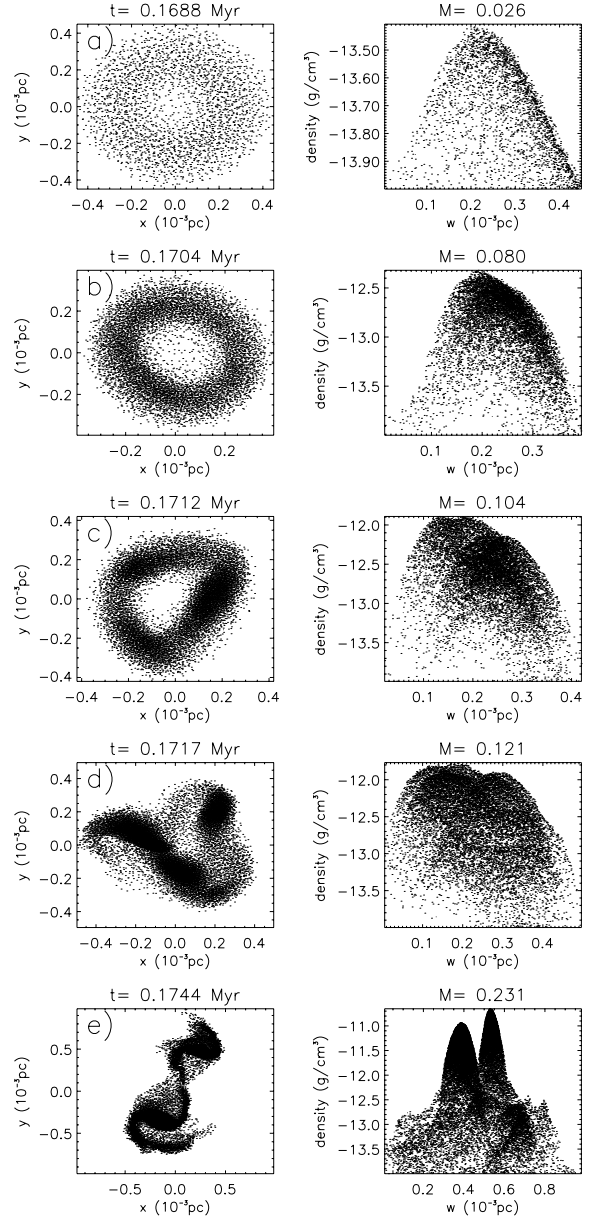


Figure 7. Disc instability in the central $\sim 10^{-3}$ pc for $\phi = 0.1$ (very rapid compression) and $\beta_0 = 0.02$. The left-hand column shows particle positions projected on to the $z = 0$ plane. The right-hand column shows $\log_{10}[\rho_i]$ plotted against equatorial coordinate w_i , for each particle i having density above $10^{-14} \text{ g cm}^{-3}$ and the solid line shows $\bar{\rho}(w)$, the mean density interior to radius w , as defined in equation (A31). Five time-steps are shown, $t = 0.1688, 0.1704, 0.1712, 0.1717, 0.1744$ Myr. The mass on top of the panels is in M_\odot . Fragmentation occurs via a ring which initially breaks up into three pieces; two of these merge, and the end-result is two protostars.

isolation, whilst enforcing axisymmetry. The ring quickly settles into an equilibrium in which ~ 17 per cent of its mass has density below $\rho_0/10$, and this mass carries ~ 33 per cent of the angular momentum of the ring. We conclude that it is the accretion shock which gives the ring a sharply defined outer boundary, and maintains its high mean density and high specific angular momentum.

Thirdly, once the ring density becomes higher than the mean density, its gravity starts to attract infalling material away from the centre, thereby further enhancing its density contrast (see Fig. 7b, $t = 0.1704$ Myr). The ring is established so quickly that there is

insufficient time for the symmetry-breaking instabilities which could redistribute angular momentum and deliver material into a central primary protostar.

Self-gravitating rings are very unstable to non-axisymmetric instabilities (Ostriker 1964; Norman & Wilson 1978), and within a few orbital periods of its formation it breaks up into three massive fragments (Fig. 7c, $t = 0.1712$ Myr). At the same time these fragments start to interact dynamically (Fig. 7d, $t = 0.1717$ Myr). Two of them merge, and the end result is a binary (Fig. 7e, $t = 0.1744$ Myr). The object located at $x = -0.1 \times 10^{-3}$ pc, $y = -0.3 \times 10^{-3}$ pc in Fig. 7(e) has mass $\simeq 0.08 M_{\odot}$; the object at $x = +0.3 \times 10^{-3}$ pc, $y = +0.6 \times 10^{-3}$ pc has mass $\simeq 0.06 M_{\odot}$. Both objects are still accreting and have small discs with spiral patterns around them. Ring fragmentation tends to produce objects of comparable mass (as here), in contrast to disc instability where the secondary protostars formed for $\phi = 0.3$ tend to be four or five times less massive than the primary.

In order to demonstrate the importance of the ram pressure of the accretion shock, we have performed a simple numerical experiment. We first extract the ring structure displayed in Fig. 7(b) (i.e. we select particles having a density larger than $\rho_0/10$). Then we let this ring evolve in isolation, first with no external pressure, and second with an external pressure equal to the average thermal pressure of its particles (i.e. comparable to the ram pressure of the infalling gas). In the first case (no external pressure, left-hand column of Fig. 8), there is no permanent fragmentation. Transient structures develop in the ring, but, because they lack a confining pressure, they are diffuse, and they merge to form a single central protostar. The rest of the material ends up in an expanding disc. A similar result has been reported by Bonnell (1994), who finds that the disc which forms around his central primary protostar only fragments if envelope material continues to fall in on to the disc. In the second case (external pressure approximately equal to ram pressure, right-hand column of Fig. 8), the evolution is broadly similar to that presented in Fig. 7. The ring breaks up into three fragments, and subsequently two of them merge. This indicates that the confinement of the ring by the ram pressure of the infalling gas plays an important role in promoting fragmentation.

4.4 Stronger rotation

In order to investigate the effect of higher rotation on fragmentation, we have performed numerical simulations with $\beta_0 = 0.05$. The results for $\phi = 3$ and $\beta_0 = 0.05$ are presented in Fig. 9. In this case the central density first rises above $\rho_0/3$ at $t \simeq 0.7237$ Myr, and the time-steps shown are 2000, 3000, 4000, 5000 and 7000 yr after this. The principal effect of higher angular momentum is to increase the mass and extent of the disc at the expense of the central primary protostar (relative to the case $\phi = 3$, $\beta_0 = 0.02$), so the disc is more unstable. As a result, the spiral arms become self-gravitating and condense out to produce two secondary companions.

We infer that, in the parameter space that we have explored here (and that we expect to be representative of real star-forming cores), both rotation (higher β_0) and rapid compression (higher ϕ) promote fragmentation. This is in accordance with the analysis in the appendix. For higher ϕ and β_0 the material impinging on the accretion shock at the edge of the disc has higher density, and therefore the density in the outer parts of the disc is higher. In addition, for higher ϕ and β_0 , this material is delivered to the outer parts of the disc more rapidly, so there is less time for disc material to redistribute angular momentum, and the mass of the central primary protostar is lower. Therefore, as demonstrated in the appendix, the accretion

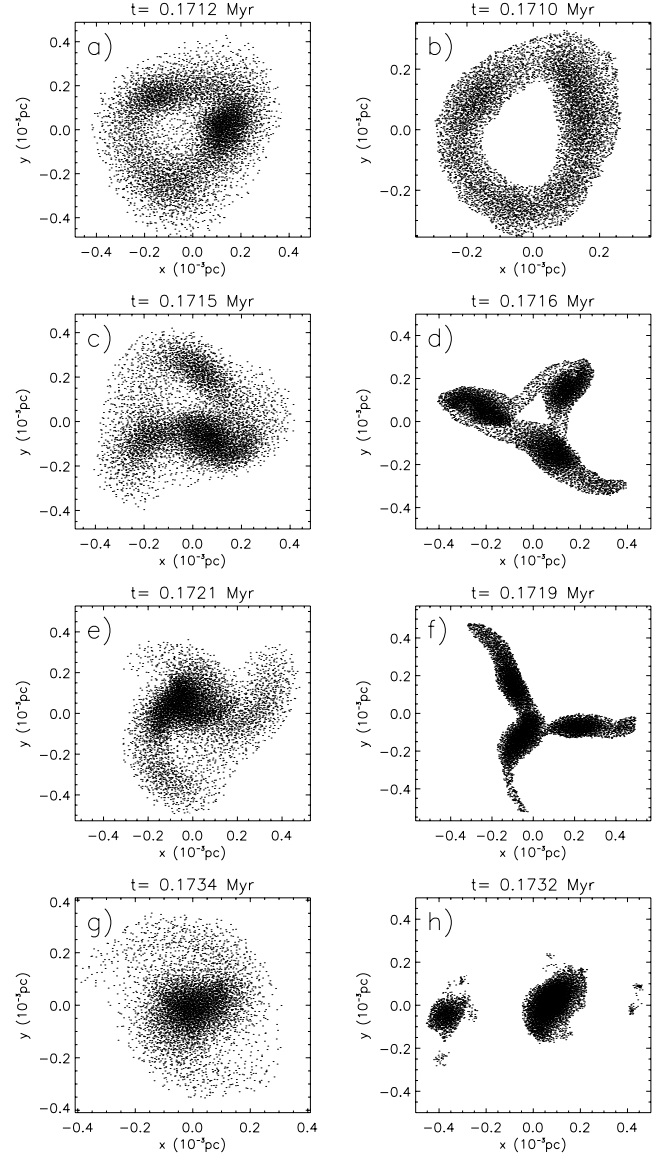


Figure 8. Evolution of the ring structure displayed in Fig. 7(b) when the envelope is removed. The left-hand column shows the evolution when there is no external pressure. With no external pressure, a single central protostar forms, the outer parts of the ring expand, and there is no fragmentation. The right-hand column shows the evolution when the external pressure is approximately equal to the ram pressure of the infalling gas. In this case, the evolution is very similar to the full simulation displayed in Fig. 7.

and local time-scales are reduced relative to the global time-scale, and the disc is more unstable against fragmentation.

5 SUMMARY AND DISCUSSION

We have investigated the effect of compression on the collapse and fragmentation of a rotating core.

Most of the conclusions of Paper I, concerning the large-scale dynamics of the collapsing core, are still valid. In particular, the increase in external pressure drives a compression wave into the core. The compression wave leaves in its wake a velocity field very similar to those recently inferred for prestellar cores, from observations of asymmetric molecular-line profiles. Tafalla et al. (1998) estimated inflow at ~ 0.10 km s $^{-1}$ in the outer layers of L1544, and Williams et al. (1999) found inflow at ~ 0.08 km s $^{-1}$ further in. Lee et al.

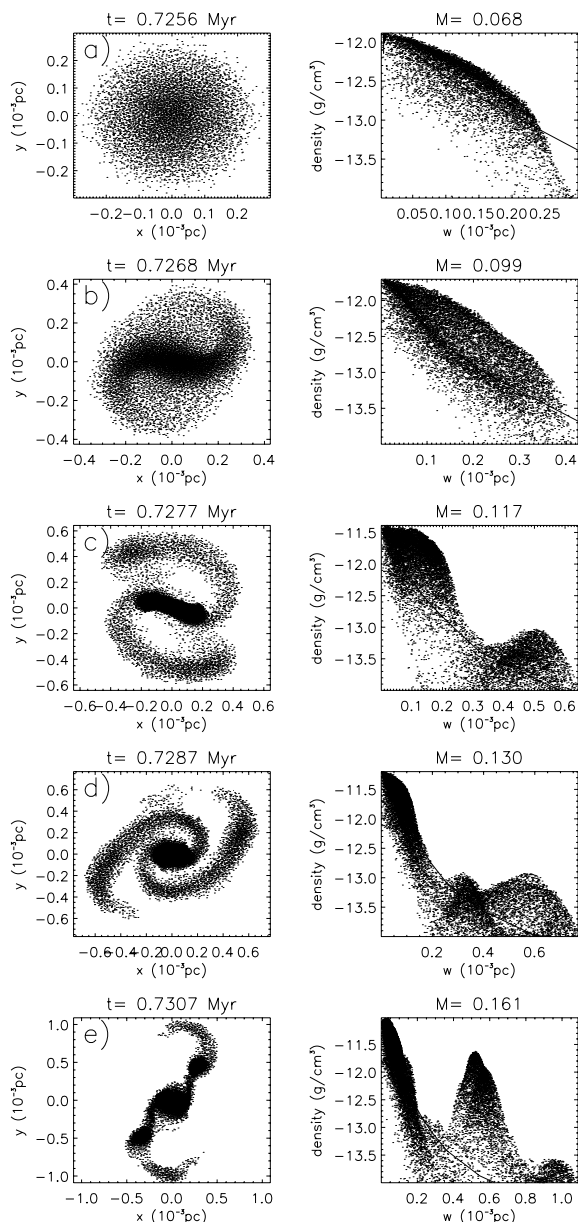


Figure 9. Disc instability in the central $\sim 10^{-3}$ pc for $\phi = 3$ (slow compression) and $\beta_0 = 0.05$ (above average rotation). The left-hand column shows particle positions projected on to the $z = 0$ plane. The right-hand column shows $\log_{10}[\rho_i]$ plotted against equatorial coordinate w_i , for each particle i having density above 10^{-14} g cm $^{-3}$, and the solid line shows $\bar{\rho}(w)$, the mean density interior to radius w , as defined in equation (A31). Five time-steps are shown, $t = 0.7256, 0.7268, 0.7277, 0.7287, 0.7307$ Myr. The mass on top of the panels is in M_\odot . Fragmentation of the disc around the primary protostar produces two further protostars.

(1999) detected inflow velocities ranging from 0.04 to 0.10 km s $^{-1}$ in several other prestellar cores. Our models generate comparable inflow velocities for ϕ in the range 10–1, i.e. slow to intermediate compression. Interestingly, in regions like Perseus and ρ Ophiucus, where star formation is triggered more violently, cores with significantly higher infall velocities have been observed. For example, Di Francesco et al. (2001) detected velocities of ~ 0.5 – 0.7 km s $^{-1}$ in the Class 0 protostars of NGC 1333 IRAS 4, suggesting that very fast compression may have occurred in this region.

The fundamental difference from Paper I is that because the cores we simulate here have rotation, the inflowing material does not all converge directly on to the central primary protostar. Instead, a large fraction of it first collects in an accretion disc around the CPP, and instabilities in the outer parts of this disc may then lead to fragmentation producing additional protostars. As noted by Larson (2002), the critical factors determining the stability of the outer disc are (i) its mass and density and (ii) the speed with which it is assembled: *a quickly assembled, massive, dense outer disc is unstable against fragmentation.*

We show numerically – and, in the Appendix, semi-analytically – that the density in the envelope is larger for faster compression, and for larger β_0 . These effects may already have been observed. In cores belonging to the relatively quiescent star formation region Taurus, the inflow velocities are compatible with slow compression, and the density is close to the density of the singular isothermal sphere. Conversely, in cores belonging to more active star formations regions, the inflow velocities appear to be supersonic, and the densities are approximately one order of magnitude higher than the density of the SIS (Motte & André 2001; André et al. 2003). This accords with the predictions of the analysis in the appendix.

Except in the case of very rapid compression, the low angular momentum material arriving in the centre of the core goes directly into the CPP, and the high angular momentum material forms an accretion disc round the CPP. If the compression is more rapid, this has a number of effects which tend to render the disc more unstable. First, the material accreting on to the outer parts of the disc arrives with higher density, and therefore the density in the outer disc – following compression in the accretion shock at the edge of the disc – is also higher. Secondly, material is delivered into the outer parts of the disc more rapidly, and therefore these outer parts become more massive. Thirdly, there is less time for the gravitational torques associated with symmetry-breaking instabilities in the disc (the same instabilities which lead to fragmentation) to redistribute angular momentum and thereby facilitate the continuing growth of the CPP. The combination of a massive, dense outer disc and a low-mass CPP makes the outer disc unstable against fragmentation, spawning secondary protostars with masses typically four or five times lower than the CPP.

For very rapid compression there is no CPP; all the material flows into the disc, and it is so concentrated towards the edge that it is more accurately described as a ring. The ring then fragments into two or three protostars of comparable mass.

For more rapid rotation ($\beta_0 = 0.05$) the outer disc is even more massive in comparison to the CPP, even more extended, and therefore even more prone to fragment.

In the appendix we analyse the structure of the inflowing envelope, and its consequences for the stability of the central disc. This analysis explains why higher rotation (large β_0) and more rapid compression (small ϕ) promote fragmentation and the formation of multiple protostars.

ACKNOWLEDGMENTS

PH and APW gratefully acknowledge the support of an European Commission Research Training Network under the Fifth Framework Programme (No. HPRN-CT2000-00155). APW and SPG gratefully acknowledge the support of a PPARC Research Assistantship (No. PPA/G/S/1998/00623). PH gratefully acknowledges the support of a CNES fellowship. We thank Arnaud Belloche and Phillippe Andre for stimulating discussions.

REFERENCES

- Abergel A., Bernard J.P., Boulanger F., Cesarsky C., Desert F.X., Falgarone E., Lagache G., Perault M., 1996, *A&A*, 315, L329
- André P., Ward-Thompson D., Barsony M., 2000, in Mannings V., Boss A.P., Russell S.S., eds, *Protostars and Planets IV*. Univ. of Arizona Press, Tucson, p. 59
- André P., Bouwman J., Belloche A., Hennebelle P., 2003, in Curry C.L., Fich M., eds, *Chemistry as a Diagnostic of Star Formation*, in press
- Arcoragi J.-P., Bonnell I., Martel H., Benz W., Bastien P., 1991, *ApJ*, 380, 476
- Bacmann A., André P., Puget J.-L., Abergel A., Bontemps S., Ward-Thompson D., 2000, *A&A*, 361, 555
- Balsara D.S., 1995, *J. Chem. Phys.*, 121, 357
- Bastien P., 1983, *A&A*, 119, 109
- Bastien P., Arcoragi J.-P., Benz W., Bonnell I., Martel H., 1991, *ApJ*, 378, 255
- Bate M.R., Burkert A., 1997, *MNRAS*, 288, 1060
- Bate M.A., Bonnell I.A., Price N.M., 1995, *MNRAS*, 277, 362
- Belloche A., André P., Despois D., Blinder S., 2002, *A&A*, 393, 927
- Bodenheimer P., Burkert A., Klein R.I., Boss A.P., 2000, in Mannings V., Boss A.P., Russell S.S., eds, *Protostars and Planets IV*. Univ. of Arizona Press, Tucson, p. 675
- Bonnell I.A., 1994, *MNRAS*, 269, 837
- Bonnell I., Bastien P., 1991, *ApJ*, 374, 610
- Bonnell I., Bastien P., 1992, *ApJ*, 401, 654
- Bonnell I.A., Bate M.R., 1994, *MNRAS*, 271, 999
- Bonnell I., Martel H., Bastien P., Arcoragi J.-P., Benz W., 1991, *ApJ*, 377, 553
- Bonnell I., Arcoragi J.-P., Martel H., Bastien P., 1992, *ApJ*, 400, 579
- Bonnell I.A., Bate M.R., Price N.M., 1996, *MNRAS*, 279, 121
- Bontemps S., André P., Terebey S., Cabrit S., 1996, *A&A*, 311, 858
- Boss A.P., 1993, *ApJ*, 410, 157
- Boss A.P., 1996, *ApJ*, 468, 231
- Boss A.P., Bodenheimer P., 1979, *ApJ*, 234, 289
- Boss A.P., Myhill E., 1995, *ApJ*, 451, 218
- Boss A.P., Fisher R.T., Klein R.I., McKee C.F., 2000, *ApJ*, 528, 325
- Burkert A., Bodenheimer P., 1993, *MNRAS*, 264, 798
- Burkert A., Bodenheimer P., 1996, *MNRAS*, 280, 1190
- Burkert A., Bate M., Bodenheimer P., 1997, *MNRAS*, 289, 497
- Cassen P., Moosman A., 1981, *Icarus*, 48, 353
- Cha S.-H., Whitworth A.P., 2003, *MNRAS*, 340, 91
- Chandrasekhar S., 1969, *Ellipsoidal Figures of Equilibrium*. New Haven, Yale Univ. Press
- Di Francesco J., Myers P.C., Wilner D.J., Ohashi N., Mardones D., 2001, *ApJ*, 562, 770
- Duquennoy A., Mayor M., 1991, *A&A*, 248, 485
- Durisen R.H., Gingold R.A., Tohline J.E., Boss A.P., 1986, *ApJ*, 305, 281
- Elmegreen B.G., 2000, *ApJ*, 530, 277
- Fisher D.A., Marcy G.W., 1992, *ApJ*, 396, 178
- Ghez A.M., McCarthy D.W., Patience J.L., Beck T.L., 1997, *ApJ*, 481, 378
- Goodman A.A., Benson P.J., Fuller G.A., Myers P.C., 1993, *ApJ*, 406, 528
- Greene T.P., Wilking B.A., André P., Young E.T., Lada C.J., 1994, *ApJ*, 434, 614
- Hachisu I., Eriguchi Y., 1984, *A&A*, 140, 259
- Hachisu I., Eriguchi Y., 1985, *A&A*, 143, 355
- Hennebelle P., 2003, *A&A*, 397, 381
- Hennebelle P., Whitworth A.P., Gladwin P.P., André P., 2003, *MNRAS*, 340, 870 (Paper I)
- Kenyon S.J., Hartmann L.W., 1995, *ApJS*, 101, 117
- Kitsionas S., Whitworth A.P., 2002, *MNRAS*, 330, 129
- Larson R.B., 1969, *MNRAS*, 145, 271
- Larson R.B., 2002, *MNRAS*, 332, 155
- Lee C.W., Myers P.C., Tafalla M., 1999, *ApJ*, 526, 788
- Lyttleton R.A., 1953, *The Stability of Rotating Liquid Masses*. Cambridge Univ. Press, Cambridge
- Masunaga H., Inutsuka S., 2000, *ApJ*, 531, 350
- Miyama S.M., 1992, *PASJ*, 44, 193
- Miyama S.M., Hayashi C., Narita S., 1984, *ApJ*, 279, 621
- Monaghan J.J., 1992, *ARA&A*, 30, 543
- Monaghan J.J., 1994, *A&A*, 420, 692
- Motte F., André P., 2001, *A&A*, 365, 440
- Myhill E.A., Kaula W.M., 1992, *ApJ*, 386, 578
- Nelson R.P., Papaloizou J.C.B., 1993, *MNRAS*, 265, 905
- Norman M.L., Wilson J.R., 1978, *ApJ*, 224, 497
- Ostriker J.P., 1964, *ApJ*, 140, 1067
- Ostriker J.P., Bodenheimer P., 1973, *ApJ*, 180, 171
- Padoan P., Nordlund A., 2002, *ApJ*, 576, 870
- Penston M.V., 1969, *MNRAS*, 144, 425
- Saigo K., Hanawa T., 1998, *ApJ*, 493, 342
- Shu F.H., 1977, *ApJ*, 214, 488
- Sigalotti L., Klapp J., 1997, *ApJ*, 474, 710
- Sigalotti L., Klapp J., 2001, *A&A*, 378, 165
- Stahler S.W., Korycansky D.G., Brothers M.J., Toulma J., 1994, *ApJ*, 431, 341
- Tafalla M., Mardones D., Myers P.C., Caselli P., Bachiller R., Benson P.J., 1998, *ApJ*, 504, 900
- Tohline J.E., 1980, *ApJ*, 236, 160
- Tohline J.E., 1981, *ApJ*, 248, 717
- Tohline J.E., 1982, *Fundam. Cosmic Phys.*, 8, 1
- Truelove J.K., Klein R.I., McKee C.F., Howell L.H., Greenough J.A., Woods D.T., 1997, *ApJ*, 489, L179
- Truelove J.K., Klein R.I., McKee C.F., Howell L.H., Greenough J.A., Woods D.T., 1998, *ApJ*, 495, 821
- Tsuribe T., Inutsuka S., 1999a, *ApJ*, 526, 307
- Tsuribe T., Inutsuka S., 1999b, *ApJ*, 523, L155
- Whitworth A.P., Summers D., 1985, *MNRAS*, 214, 1
- Whitworth A.P., Chapman S.J., Bhattal A.S., Disney M.J., Pongratic H., Turner J.A., 1995, *MNRAS*, 277, 727
- Williams J.P., Myers P.C., Wilner D.J., Di Francesco J., 1999, *ApJ*, 513, L61

APPENDIX: ANALYTICAL PREDICTIONS

In the appendix we analyse the structure of the inflowing envelope, and its consequences for the stability of the central disc. This analysis explains why higher rotation (large β_0) and more rapid compression (small ϕ) promote fragmentation and the formation of multiple protostars.

Here, we develop an analytic description of the structure of the inflowing envelope and its consequences for the stability of the disc which forms around the central primary protostar (or, in the case of very rapid compression, the ring structure which forms around a central rarefaction), with a view to understanding how disc fragmentation is affected by changes in the initial rotation (β_0) and the rate of compression (ϕ). The formation and evolution of a disc embedded in a rotating and collapsing core has already been investigated and elegantly described in seminal papers by (Cassen & Moosman 1981) and Stahler et al. (1994). However, these authors assume that the core collapses according to the inside-out model of Shu (1977), starting from a singular isothermal sphere. Here we wish to consider the case of dynamically triggered collapse, which is necessarily from the outside-in.

Four features of the collapse are crucial to this discussion. First, the polar density profile $\rho(w = 0, z)$ is close to the density profile of the SIS, whereas the equatorial density profile $\rho(w, z = 0)$ is significantly higher. Secondly, the maximum value of the inward equatorial velocity $|v_w(w, z = 0)|_{\max}$ increases monotonically with time until the disc forms, after which it is approximately constant. Thirdly, this asymptotic maximum equatorial velocity (which determines the strength of the accretion shock at the edge of the disc) depends only weakly on the rate of compression ϕ . Fourthly, the strength of the accretion shock at the edge of the disc has an important influence on the stability of the disc. By analysing these

effects, we can estimate the different time-scales controlling fragmentation, and hence interpret the results reported in Section 4.

A1 Density profile

According to the numerical results displayed on Fig. 2 the equatorial density profile $\rho(w, z = 0)$ depends on the rate of compression ϕ and on the initial rotation β_0 .

A1.1 The effect of external pressure

The first effect (rapid compression leading to large equatorial density) can be understood qualitatively by reference to the self-similar solutions studied by Whitworth & Summers (1985). In these solutions, the density at large radius converges to u_∞/r^2 . Whitworth & Summers (1985) show that the stronger the compression wave being driven into the core, the faster the collapse and the higher u_∞ . The slowest collapse corresponds to Shu's inside-out collapse from a singular isothermal sphere (Shu 1977) and has $u_\infty = 2$. The Larson–Penston solution (Larson 1969; Penston 1969) corresponds to collapse from a centrally flat density profile, induced by a strong compression wave, and has $u_\infty \simeq 7$.

We therefore assume that the density profile can be approximated by

$$\rho(r) \simeq \frac{A}{r^2}, \quad (\text{A1})$$

where A is a constant. This assumption is justified both by the numerical results presented in Fig. 2 and by the asymptotic form of the similarity solutions obtained by Whitworth & Summers (1985). Significant departures from $\rho(r) \propto r^{-2}$ are confined to the inner parts of the core which contain very little of the total mass.

If R_c is the core radius, then the core pressure at this point must be equal to the external pressure, P_{ext} , i.e.

$$\frac{AC_s^2}{R_c^2} = P_{\text{ext}}. \quad (\text{A2})$$

Mass conservation requires

$$4\pi R_c A = M_c - M_*, \quad (\text{A3})$$

where M_c is the initial core mass and M_* is the mass of the central primary protostar. As long as $M_* \ll M_c$, as it is when the disc first forms, M_* can be neglected, so

$$A = P_{\text{ext}}^{1/3} \left(\frac{M_c}{4\pi C_s} \right)^{2/3}. \quad (\text{A4})$$

Recalling that the density of a singular isothermal sphere is

$$\rho_{\text{SIS}} = \frac{C_s^2}{2\pi G r^2}, \quad (\text{A5})$$

we can write

$$\frac{\rho(r)}{\rho_{\text{SIS}}(r)} \simeq \frac{2\pi G A}{C_s^2} \simeq \left(\frac{P_{\text{ext}}}{P_0} \right)^{1/3}, \quad (\text{A6})$$

where $P_0 \sim C_s^8/G^3 M_c^2$ is the pressure at the boundary of the core before compression starts. From the numerical results for $\phi = 3$, $\rho_{\text{ext}} \simeq 10^{-18.9} \text{ g cm}^{-3}$, giving $\rho/\rho_{\text{SIS}} \simeq 1.42$; whilst for $\phi = 0.3$, $\rho_{\text{ext}} \simeq 10^{-18.5} \text{ g cm}^{-3}$, giving $\rho/\rho_{\text{SIS}} \simeq 1.93$. The dotted lines on Fig. 2 demonstrate that these predictions are in good agreement with the numerical results.

A1.2 The effect of rotation

The similarity equations describing self-gravitating collapse have been extended to include rotation by Saigo & Hanawa (1998) for disc geometry, and by Hennebelle (2003) for filamentary geometry. However, the geometry assumed in these treatments is significantly different from the geometry that we are considering here. In order to investigate analytically the effect of rotation on the density profile, we simply assume that the core is close to equilibrium, so that in the equatorial direction

$$-\frac{C_s^2}{\rho} \frac{\partial \rho}{\partial w} + \frac{v_\theta^2}{w} + \frac{\partial \Phi}{\partial w} \simeq 0. \quad (\text{A7})$$

If we now neglect departures from spherical symmetry, and substitute

$$\rho(w, z = 0) \simeq \frac{A}{w^2}, \quad (\text{A8})$$

so that $\partial \Phi / \partial w \simeq -4\pi G A / w$, we obtain

$$A \simeq \frac{C_s^2}{2\pi G} \left(1 + \frac{v_\theta^2}{2C_s^2} \right). \quad (\text{A9})$$

and hence

$$\frac{\rho(w, z = 0)}{\rho_{\text{SIS}}(w)} \simeq \frac{2\pi G A}{C_s^2} \simeq \left(1 + \frac{v_\theta^2}{2C_s^2} \right). \quad (\text{A10})$$

If $v_\theta = 0$, the SIS density profile is recovered. In general, v_θ is finite, but not constant, and so A is not constant either. However, the variation of v_θ with w is always much weaker than w^{-2} , so to a first approximation we can treat A as constant. Equation (A10) explains why the equatorial density profile $\rho(w, z = 0)$ is higher than the SIS density profile, and why the increase is greatest in the inner parts of the core, where v_θ is greatest (see Fig. 1).

In order to test the predictions of equation (A10), Fig. 2 compares the density profiles obtained in simulations with $\phi = 3$ or 0.3 and $\beta_0 = 0.02$ (thin dashed lines) with the density profiles obtained in simulations with no rotation (dotted lines), but then multiplied by the factor $1 + v_\theta^2/2C_s^2$ from equation (A10) to give the thick dashed lines. The comparison is made at the time when the maximum density first reaches ρ_0 , and values of v_θ are taken from the rotating simulations represented by the thin dashed lines. In general, the agreement between the two dashed lines (thin and thick) on Fig. 2 is good, particularly for large values of ϕ .

Combining equations (A6) and (A10), we propose that by the time the central primary protostar forms, the equatorial density profile can be approximated by

$$\rho(w, z = 0) = \delta \rho_{\text{SIS}}(w) = \frac{\delta C_s^2}{2\pi G w^2}, \quad (\text{A11})$$

$$\delta \simeq \left(\frac{P_{\text{ext}}}{P_0} \right)^{1/3} \left(1 + \frac{v_\theta^2}{2C_s^2} \right). \quad (\text{A12})$$

δ is the factor by which the density in the inflowing gas in the envelope is enhanced by the combined effect of compression and rotation. In the outer parts of the envelope, the rotational velocity is normally very small compared with the speed of sound, and so there the overdensity (relative to the SIS) is dominated by the effect of compression. However, in the inner parts of the envelope the rotation velocity becomes large, compared with the speed of sound, and both effects are then important.

A2 Infall velocity

Now consider a parcel of gas, falling inwards on to the disc. Its acceleration is the sum of gravitational and centrifugal terms; we neglect the effect of thermal pressure. We assume that the mass of the disc contained within radius w is given by

$$M_w \simeq \pi \rho_0 w_0^2 \ell, \quad (\text{A13})$$

where ρ_0 is the initial density of the core (assumed to be uniform, for simplicity), w_0 is the initial position of the gas parcel which is now (at time t) located at w , and ℓ is the initial height of the cylinder that has now flattened into the disc out to radius w . Let Ω_0 be the initial angular speed of the core. Then the equation of motion for the parcel is

$$\begin{aligned} \frac{d^2 w}{dt^2} &\simeq -\frac{\Gamma G M_w}{w^2} + \frac{w_0^4 \Omega_0^2}{w^3} \\ &\simeq -\frac{\Gamma \pi G \rho_0 \ell w_0^2}{w^2} + \frac{w_0^4 \Omega_0^2}{w^3}, \end{aligned} \quad (\text{A14})$$

where Γ is a geometrical factor of the order of unity. Equation (A14) can be integrated to give

$$\left(\frac{dw}{dt}\right)^2 \simeq \frac{2\pi\Gamma G \rho_0 \ell w_0^2}{w} - \frac{w_0^4 \Omega_0^2}{w^2} + v_0^2, \quad (\text{A15})$$

where v_0 is the initial velocity and depends on w_0 and β .

It follows that the maximum equatorial velocity, $|v_w(w, z=0)|_{\max}$, is reached at

$$w_{\max} \simeq \frac{w_0^2 \Omega_0^2}{\pi \Gamma G \rho_0 \ell}, \quad (\text{A16})$$

and this is in effect the position of the accretion shock at the edge of the disc, where the parcel of gas that we are following accretes on to the disc. Therefore, the edge of the disc is at

$$w_{\text{edge}} \simeq \frac{w_0^2 \Omega_0^2}{\pi \Gamma G \rho_0 \ell}. \quad (\text{A17})$$

Combining equations (A15) and (A16), the maximum inward equatorial velocity reached by the parcel of gas as it impinges on the accretion shock at the edge of the disc is

$$\begin{aligned} v_{\text{acc}} &\equiv \left| \frac{dw}{dt} \right|_{\max} \\ &\simeq \left[\left(\frac{\Gamma \pi G \rho_0 \ell}{\Omega_0} \right)^2 + v_0^2 \right]^{1/2} \\ &\simeq \frac{\Gamma \pi G \rho_0 \ell}{\Omega_0}. \end{aligned} \quad (\text{A18})$$

Equation (A18) shows that v_{acc} depends only on $\Sigma_0 = \rho_0 \ell$ (i.e. the initial cloud surface density or some fraction thereof) and not on w_0 . By the time the disc forms, the cloud is significantly flattened and this quantity is almost constant. Consequently, the variation of v_{acc} is expected to be small.

Substituting from equation (A17) in equation (A13), we obtain an expression for the total mass of the disc

$$M_{\text{disc}} = \frac{\pi^2 \Gamma G \rho_0^2 \ell^2 w_{\text{edge}}}{\Omega_0^2}. \quad (\text{A19})$$

We reiterate that these equations are valid only if the thermal pressure can be neglected. In particular, if β_0 is too small then the gas parcel becomes adiabatic ($\rho > \rho_0$) before it reaches the disc. In the cases treated here, the gas is still isothermal when it first

encounters the accretion shock at the edge of the disc (since its density is $\sim 0.1 \rho_0$, see Figs 1 and 3). Thus neglecting the thermal pressure is acceptable, and the ram pressure of the gas flowing into the disc ($\simeq \rho v_{\text{acc}}^2$) is larger than its thermal pressure ($\simeq \rho C_0^2$).

Since the values of v_{acc} obtained in Section 3 appear to depend only weakly on the rate of compression (ϕ), we infer that $v_{\text{acc}} \gg v_0$. Therefore, neglect of v_0 in the final form of equation (A18) is justified. It follows that for two different values of β_0 ,

$$\frac{v_{\text{acc}}(\beta_2)}{v_{\text{acc}}(\beta_1)} \simeq \left(\frac{\beta_1}{\beta_2} \right)^{1/2} \left(\frac{\Gamma_2 \ell_2}{\Gamma_1 \ell_1} \right), \quad (\text{A20})$$

since $\Omega_0 \propto \beta_0^{1/2}$.

In order to compare the predictions of equation (A18) with the numerical results, we need to estimate the combination $\rho_0 \ell / \Omega_0$. For the uniform-density, uniformly rotating cloud from which our initial conditions are generated, we can write

$$\frac{\rho_0 \ell}{\Omega_0} \lesssim \frac{3M_c}{4\pi R_c^2 \Omega_0}, \quad (\text{A21})$$

where M_c is the core mass and R_c the core radius. Combining equations (A18) and (A21), we obtain

$$v_{\text{acc}} \lesssim \frac{3\Gamma G M_c}{4R_c^2 \Omega_0} \simeq 1.2 \text{ km s}^{-1}. \quad (\text{A22})$$

Although this inequality has been derived assuming a uniform-density, uniformly rotating core, it is still valid for our simulations. That is because the stretching which creates the initial conditions for our simulations (by converting a uniformly rotating uniform-density core into a differentially rotating BE sphere) conserves both the core mass M_c , and the specific angular momentum $R_c^2 \Omega_0$. From Figs 1 and 3 we see that in the simulations $v_{\text{acc}} \sim 0.8 \pm 0.1 \text{ km s}^{-1}$. We note that equation (A22) gives an upper limit on v_{acc} because $\ell \lesssim R_c$, and because we have neglected the thermal pressure in deriving equation (A18).

In order to compare the predictions of equation (A20) with the numerical results, we have performed a simulation with $\beta_0 = 0.05$ and $\phi = 3$ in which we find $v_{\text{acc}}(0.05) \simeq 0.55 \text{ km s}^{-1}$, as compared with $v_{\text{acc}}(0.02) \simeq 0.85 \text{ km s}^{-1}$ in the simulation with $\beta_0 = 0.02$ and $\phi = 3$, giving a ratio

$$\frac{v_{\text{acc}}(0.05)}{v_{\text{acc}}(0.02)} \Big|_{\text{simulation}} \simeq 0.65. \quad (\text{A23})$$

If we can neglect variations in Γ and ℓ , equation (A20) predicts a ratio

$$\frac{v_{\text{acc}}(0.05)}{v_{\text{acc}}(0.02)} \Big|_{\text{analysis}} \simeq \left(\frac{0.02}{0.05} \right)^{1/2} \simeq 0.63. \quad (\text{A24})$$

In view of all the approximations and assumptions made in deriving this result, the extreme closeness of the agreement between equations (A23) and (A24) must be somewhat fortuitous, but it suggests that our analysis is a reliable guide to trends.

Finally, we can show that the tangential velocity of the parcel of gas which is about to impinge on the edge of the disc, $v_{\text{tang}} \equiv v_\theta(w = w_{\text{edge}}, z = 0)$ should be approximately constant. The specific angular momentum of the parcel is $w_0^2 \Omega_0$, so its tangential velocity is

$$v_{\text{tang}} \simeq \frac{w_0^2 \Omega_0}{w_{\text{edge}}} = \frac{\pi \Gamma G \rho_0 \ell}{\Omega_0}, \quad (\text{A25})$$

where we have obtained the second expression on the right-hand side of equation (A25) by substituting from equation (A17). Comparing equation (A25) with equation (A18), we see that

$$v_{\text{tang}} \simeq v_{\text{acc}}, \quad (\text{A26})$$

and hence v_{tang} is approximately constant like v_{acc} . This is confirmed by the numerical results. For $\phi = 3$, the simulations give $w_{\text{edge}} = 2 \times 10^{-4}$ pc, $v_{\text{tang}} = 0.95 \text{ km s}^{-1}$ and $v_{\text{acc}} = 0.87 \text{ km s}^{-1}$ at $t = 0.611$ Myr; and $w_{\text{edge}} = 5 \times 10^{-4}$ pc, $v_{\text{tang}} = 1.00 \text{ km s}^{-1}$, and $v_{\text{acc}} = 0.85 \text{ km s}^{-1}$ at $t = 0.615$ Myr. For $\phi = 0.3$, the simulations give $w_{\text{edge}} = 3 \times 10^{-4}$ pc, $v_{\text{tang}} = 1.00 \text{ km s}^{-1}$ and $v_{\text{acc}} = 0.69 \text{ km s}^{-1}$ at $t = 0.259$ Myr; and $w_{\text{edge}} = 10 \times 10^{-4}$ pc, $v_{\text{tang}} = 0.90 \text{ km s}^{-1}$, $v_{\text{acc}} = 0.70 \text{ km s}^{-1}$ at $t = 0.262$ Myr.

8.3 Accretion shock

In order to analyse the accretion shock at the boundary of the disc, we define ρ_{edge} to be the density just inside the edge of the disc [i.e. the post-accretion-shock density, $\rho(w = w_{\text{edge}} - \epsilon, z = 0)$, where 2ϵ is the shock thickness], ρ_{acc} to be the density just outside the edge of the disc [i.e. the pre-accretion-shock density, $\rho(w = w_{\text{edge}} + \epsilon, z = 0)$], and v_{shock} to be the outward equatorial velocity of the shock relative to the centre of the core. v_{acc} is the inward equatorial velocity of the gas impinging on the shock at the edge of the disc (see equation A18). Mass conservation requires $\rho_{\text{edge}} v_{\text{shock}} < \rho_{\text{acc}} v_{\text{acc}}$, and hence $v_{\text{shock}} \ll v_{\text{acc}}$. Thus the velocity of the infalling gas in the shock frame is $\simeq v_{\text{acc}}$, and as long as the shock can be treated as isothermal, we can write

$$\rho_{\text{edge}} \simeq \rho_{\text{acc}} \left(\frac{v_{\text{acc}}}{C_s} \right)^2. \quad (\text{A27})$$

From equation (A12), we have

$$\rho_{\text{acc}} = \frac{\delta C_s^2}{2\pi G w_{\text{edge}}^2}, \quad (\text{A28})$$

and so

$$\rho_{\text{edge}} = \frac{\delta v_{w,\text{max}}^2}{2\pi G w_{\text{max}}^2}. \quad (\text{A29})$$

In the simulations presented in this paper, $v_{\text{acc}}/C_s \sim 4$ and so ρ_{edge} should be $\sim 16 \rho_{\text{acc}}$. This is corroborated by Figs 1, 3–5.

8.4 Time-scales

Disc fragmentation is an extremely non-linear process, governed both by the intrinsic structure and evolution of the disc, and its interaction with the infalling material. Given the complexity of this interaction, the formulation of a precise analytic criterion for fragmentation is probably impossible. However, useful insights can be gained by evaluating and comparing the time-scales for competing processes.

The global gravitational time-scale for the disc is related to the orbital angular frequency,

$$t_{\text{global}} \simeq \left(\frac{GM_w}{w^3} \right)^{-1/2} \simeq \left[\frac{4\pi G \bar{\rho}(w)}{3} \right]^{-1/2}, \quad (\text{A30})$$

where we have introduced

$$\bar{\rho}(w) = \frac{3M_w}{4\pi w^3}, \quad (\text{A31})$$

the mean density interior to radius w .

Similarly, the local gravitational time-scale of the disc is related to the local Jeans frequency,

$$t_{\text{local}} = [4\pi G \rho(w)]^{-1/2}, \quad (\text{A32})$$

where $\rho(w)$ is the local density in the disc.

The condition for instability is then that the local gravitational time-scale be less than the global gravitational time-scale, or equivalently

$$\left(\frac{t_{\text{local}}}{t_{\text{global}}} \right)^2 \simeq \frac{\bar{\rho}(w)}{\rho(w)} < 1. \quad (\text{A33})$$

(We note that this is essentially the same as Toomre's criterion, both for Keplerian discs, and for self-gravitating discs.)

To estimate Condition (A33) at the edge of the disc, we put $\rho(w) \rightarrow \rho_{\text{edge}}$ using equation (A29) and $\bar{\rho}(w) \rightarrow \bar{\rho}(w_{\text{edge}}) \simeq 3M_{\text{disc}}/4\pi w_{\text{edge}}^3$. Condition (A33) then becomes

$$\frac{\rho_{\text{edge}}}{\bar{\rho}(w_{\text{edge}})} \simeq \frac{2\delta w_{\text{edge}} v_{\text{acc}}^2}{3GM_{\text{disc}}} > 1. \quad (\text{A34})$$

Finally, substituting for M_{disc} , w_{edge} and v_{acc} from equations (A19), (A17) and (A18), the condition for instability (A34) becomes

$$\frac{2\Gamma\delta}{3} = \frac{2\Gamma}{3} \left(\frac{P_{\text{ext}}}{P_0} \right)^{1/3} \left(1 + \frac{v_\theta^2}{2C_s^2} \right) > 1, \quad (\text{A35})$$

where we have obtained the last expression by substituting for δ from equation (A12). This form of the condition for instability explains why more rapid compression (smaller ϕ) and more rapid initial rotation (larger β_0) both make the disc more unstable against fragmentation, by delivering higher density at the edge of the disc, i.e. higher δ .

Another important time-scale is the accretion time-scale, $t_{\text{accretion}} = M_{\text{disc}}/\dot{M}_{\text{disc}}$. Putting $\dot{M}_{\text{disc}} = 2\pi w_{\text{edge}} h \rho_{\text{acc}} v_{\text{acc}}$, where h is the vertical thickness of the layer of material flowing into the edge of the disc and $\rho_{\text{acc}} v_{\text{acc}}$ is the flux of matter into the disc, we obtain

$$t_{\text{accretion}} = \frac{M_{\text{disc}}}{2\pi w_{\text{edge}} h \rho_{\text{acc}} v_{\text{acc}}}. \quad (\text{A36})$$

Then substituting for M_{disc} , w_{edge} , ρ_{acc} and v_{acc} from equations (A19), (A17), (A28) and (A18), equation (A36) reduces to

$$t_{\text{accretion}} = \frac{\Omega_0^3 R_0^4}{\pi \Gamma^2 G \rho_0 \ell h C_s^2 \delta}. \quad (\text{A37})$$

$t_{\text{accretion}}$ is the time-scale on which mass and angular momentum are added to the disc, and it should be compared with t_{global} which is the minimum time-scale on which mass and angular momentum can be redistributed within the disc. Substituting for t_{global} from equation (A30), and again using equations (A13) and (A16) to eliminate M_{disc} and w_{edge} , we obtain

$$\frac{t_{\text{accretion}}}{t_{\text{global}}} = \frac{\pi G \rho_0 \ell w_0^2}{\Gamma^{1/2} h C_s^2 \delta}. \quad (\text{A38})$$

A small value for this ratio implies an unstable disc. ℓ/h is a geometrical factor, related to the cloud flattening, and is not easily calculated. Setting this factor aside, equation (A38) implies firstly that large δ (i.e. rapid compression and/or rapid initial rotation) promotes fragmentation, and secondly that small w_0 promotes fragmentation (i.e. fragmentation is more likely during the early stages of disc formation).

This paper has been typeset from a \LaTeX file prepared by the author.